

Classification of Chern Numbers Based on High-Symmetry Points

Yu-Hao Wan,¹ Peng-Yi Liu,¹ and Qing-Feng Sun^{1,2,*}

¹International Center for Quantum Materials, School of Physics, Peking University, Beijing 100871, China

²Hefei National Laboratory, Hefei 230088, China

The Chern number is a crucial topological invariant for distinguishing the phases of Chern insulators. Here we find that for Chern insulators with inversion symmetry, the Chern number alone is insufficient to fully characterize their topology. Specifically, distinct topological phases can be differentiated based on skyrmions at different high-symmetry points. Interfaces between these topological phases exhibit gapless helical states, which provide counter-propagating transport channels and robust quantized transport. Additionally, we identify topological transitions that do not involve changes in the Chern number but can be characterized by transitions of skyrmions between high-symmetry points. These transitions arise due to the toroidal structure of the two-dimensional Brillouin zone, which is generally applicable to two-dimensional periodic lattice system. Our research introduces new degrees of freedom for controlling topological optical transport and deepens the understanding of Chern insulators with inversion symmetry.

Over the past decade, topological insulators have been widely studied in photonic systems due to the robustness of their edge states against disorder[1–6]. Various topological states, such as the integer quantum Hall effect[4, 7–9], valley Hall effect[10–14], and spin Hall effect[15–18], have been realized in different photonic crystal systems. The topological classification theory plays a pivotal role in this investigation by characterizing the topological phases of a Hamiltonian through distinct topological indices[19]. For example, in photonic Chern insulators[7, 8, 20, 21], the Chern number serves as a topological index that distinguishes different phases[22–24]. Specifically, the absolute value of the Chern number reflects the number of topological chiral boundary states, while its sign indicates the direction of the edge flows, thereby defining the chirality of edge states.

A key result of topological classification is the inevitable appearance of gapless states at the interface between topologically distinct systems, where the topological invariant changes. These gapless states manifest as chiral modes[25–27]. The number of chiral modes at the interface of two systems with Chern numbers \mathbb{C}_1 and \mathbb{C}_2 is determined by their difference, denoted as $N_{\text{chiral}} = \mathbb{C}_1 - \mathbb{C}_2$ [25–32]. Specifically, when $\mathbb{C}_1 = \mathbb{C}_2$, no gapless states appear at the interface (top image in Fig.1(a)).

In this Letter, we discover that even for two systems with the same Chern number, gapless helical states can still appear at the interface (bottom image in Fig.1(a)), suggesting that these two systems belong to different topological classes and the Chern number alone cannot distinguish between them. We point out that in systems with inversion symmetry, those sharing the same Chern number can be further classified based on the high-symmetry points where the skyrmions are located. This novel classification scheme enhances our understanding of the topological phases of Chern insulators.

We start from a 2-bands square lattice model with inversion symmetry,

$$H = \sum_{i_x} \sum_{i_y} [c_i^\dagger \epsilon c_i + c_i^\dagger T_x c_{i+\delta x} + c_i^\dagger T_y c_{i+\delta y} + c_i^\dagger T_{\text{sec}} c_{i+\delta x+\delta y} + c_i^\dagger T_{\text{sec}} c_{i+\delta x-\delta y} + H.c.] \quad (1)$$

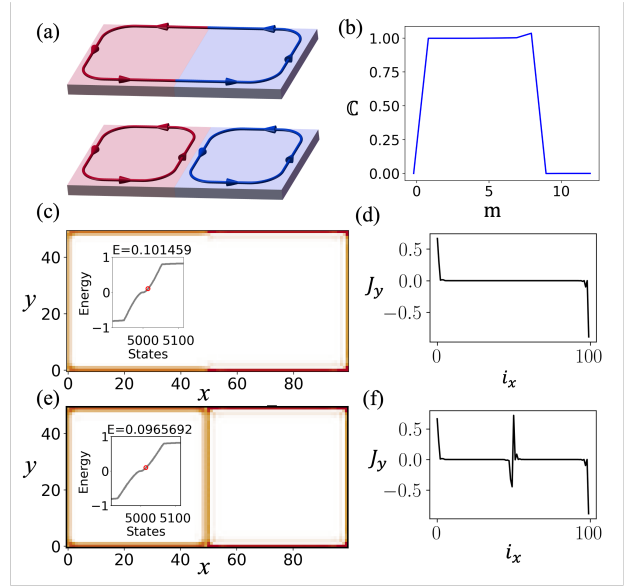


Figure 1. (a) Schematic diagram: The red and blue regions are set with different parameters, but both sides have a Chern number of 1. Chiral edge states represented by red and blue lines. Top Image: The edge states cancel each other out at the interface. Bottom Image: The helical edge states exist at the interface. (b) Chern number \mathbb{C} as a function of the mass term m . (c) Wave function distribution of the in-gap state (indicated by the red circle in the inset), with $m_l = 1$ and $m_r = 2$. Inset: Energy versus the state index. (d) Equilibrium current J_y at energy $E = 0.1$ as a function of i_x in real space. (e-f) Similar to (c-d), but with $m_l = 1$ and $m_r = 6$.

where c_i and c_i^\dagger are the annihilation and creation operators at site $\mathbf{i} = (i_x, i_y)$, respectively. Here $\delta x = (1, 0)$, $\delta y = (0, 1)$, $\epsilon = (m - 4B)\sigma_z$, nearest-neighbor hopping terms $T_x = B\sigma_z$ and $T_y = \frac{A}{2i}\sigma_y + B\sigma_z$, and the next-nearest-neighbor hopping term $T_{\text{sec}} = \frac{A}{4i}\sigma_x$. $\hat{\sigma} = (\sigma_x, \sigma_y, \sigma_z)$ represents the Pauli matrices, m is the Dirac mass term, and the parameters A and B are both set to 1 for convenience. In momentum space, the Hamiltonian reduces as

$$H(\mathbf{k}) = \mathbf{d}(\mathbf{k}) \cdot \hat{\sigma} \quad (2)$$

with $\mathbf{d}(\mathbf{k}) = (A \sin k_x \cos k_y, A \sin k_y, m + 2B(\cos k_x + \cos k_y - 2))$ and $\mathbf{k} = (k_x, k_y)$. This model is similar to the Qi-Wu-Zhang model, which is the minimal model describing the Chern insulator[33]. Both models have the same low-energy Dirac equation at the Γ point[34, 35] [see Supplemental materials (SM)[36]]. The Chern number \mathbb{C} can be calculated by integrating the Berry curvature over the Brillouin zone. Figure 1(b) shows the relationship between \mathbb{C} and the mass term m . The Chern number remains 1 within the range of m from 0 to 8, but are they all the same topological phase?

To answer this question, we consider a rectangular system with dimensions $L_x = 100$ and $L_y = 50$, where the mass term differs in the left and right halves, as shown Fig.1(a). Specifically, $m(i_x) = m_l$ for $1 \leq i_x \leq 50$ and $m(i_x) = m_r$ for $50 < i_x \leq 100$. Therefore, the system can be viewed as two blocks with different mass terms. Here, we fix $m_l = 1$. For m_r , we consider two cases: $m_r = 2$ and $m_r = 6$. The Chern number is 1 for these three masses [See Fig. 1(b)].

For the first case, where $m_l = 1$ and $m_r = 2$. By diagonalizing the Hamiltonian, we obtain the energy levels of the system and the wave function distribution of in-gap states in real space (see Fig. 1(c)), showing absence of modes at the interface between the left and right blocks, which indicates that the two blocks are in the same topological phase. Figure. 1(d) illustrates the distribution of the equilibrium current $J_y(i_x)$ (See SM for detailed calculation methods [36]). We observe that equilibrium currents almost are zero for $10 < i_x < 90$, reflecting no states at the interface.

For the second case where $m_l = 1$ and $m_r = 6$. Energy levels and the wave function distribution of the in-gap states are shown in Fig. 1(e). Surprisingly, localized modes appear at the interface between the two blocks. Additionally, the calculation of $J_y(i_x)$ shows counter-propagating currents at the interface [Fig. 1(f)], revealing the existence of the helical edge states. The gapless helical states at the interface between the two systems implies that they belong to different topological classes, despite sharing the same Chern number. In this case, the Chern number is insufficient to effectively distinguish the topology of the system.

Why does Chern number classification fail here? To answer this question, let us review the definition of the Chern number. For a two-band Bloch Hamiltonian $H(k) = \mathbf{d}(\mathbf{k}) \cdot \hat{\sigma}$, $\mathbf{d}(\mathbf{k})$ defines a vector field over the Brillouin zone, and it also gives a mapping from the Brillouin zone T_2 to S_2 [23]. The vector field $\mathbf{d}(\mathbf{k})$ forms closed surfaces in three dimension, which can wrap around the origin either positively or negatively. In this picture, the Chern number quantifies how many times the surface $\mathbf{d}(\mathbf{k})$ wrap around the origin[37].

For example, the closed surfaces of $\mathbf{d}(k)$ corresponding to Eq.(2) are illustrated in Fig. 2(a). For clarity, Fig. 2(b) shows a sectioned view of the surface $\mathbf{d}(\mathbf{k})$ from (a), with the origin $(0, 0, 0)$ marked by a green sphere. Note that the surface $\mathbf{d}(\mathbf{k})$ is divided into two parts, each being a closed surface (see SM for details on $\mathbf{d}(k)$ [36]). The mass term $m\sigma_z$ adjusts d_z , thereby shifting the surface $\mathbf{d}(k)$ in the z -direction to control which closed part wraps around the origin. When $0 < m < 4$

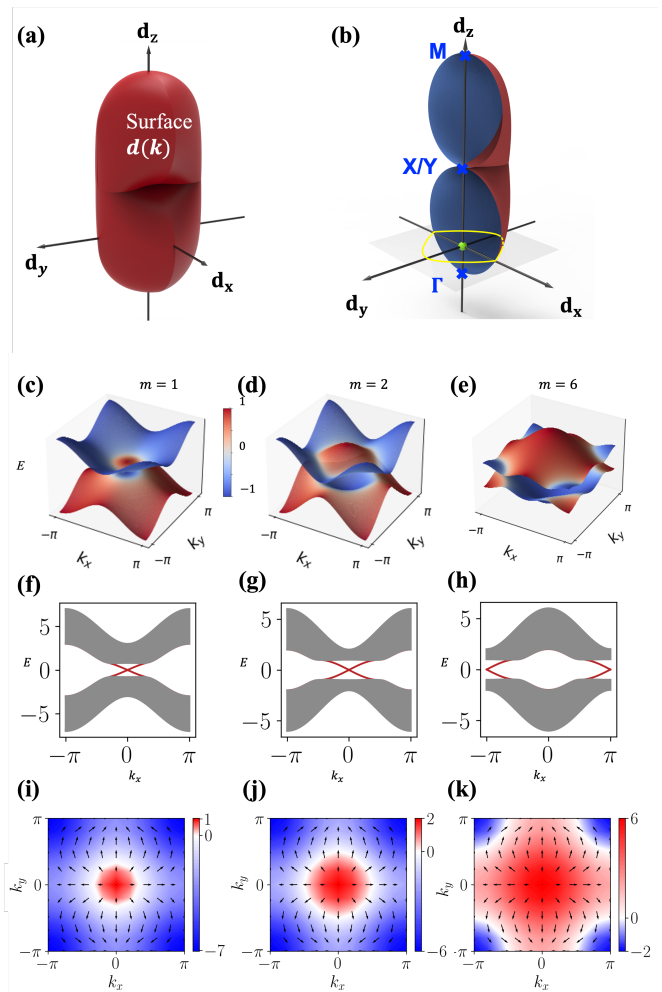


Figure 2. (a) The surface $\mathbf{d}(\mathbf{k})$ corresponding to Eq.(2) as \mathbf{k} sweeps through the whole Brillouin zone. (b) The same surface $\mathbf{d}(\mathbf{k})$ as in (a), but only the image of half of the Brillouin zone is shown for clarity. The outer surface is red, the inner surface is blue, and the origin is represented by a green sphere. The yellow line indicates the BIS. (c-e) Bulk band structure for $m = 1, 2$, and 6 . (f-h) Band diagrams of quasi-one-dimensional nanoribbons corresponding to for $m = 1, 2, 6$, with edge states marked in red. (i-k) The distribution of $\mathbf{d}(\mathbf{k})$ in the Brillouin zone for $m = 1, 2, 6$. The vector field represents the components of d_x and d_y , while color represents the d_z component.

and $4 < m < 8$, the origin is enclosed by the lower and upper parts, respectively. However, in both cases, the surface $\mathbf{d}(k)$ wraps positively around the origin once, resulting in a Chern number of 1 for both scenarios. Nevertheless, these two cases should correspond to distinct topological phases because the origin cannot be adiabatically moved from one closed region to another.

The Chern number cannot distinguish between these two topological phases because it is defined as the number of times the surface $\mathbf{d}(\mathbf{k})$ wraps around the origin[37]. In this definition, the Chern number cannot differentiate which closed surface surrounds the origin. However, the origin being sur-

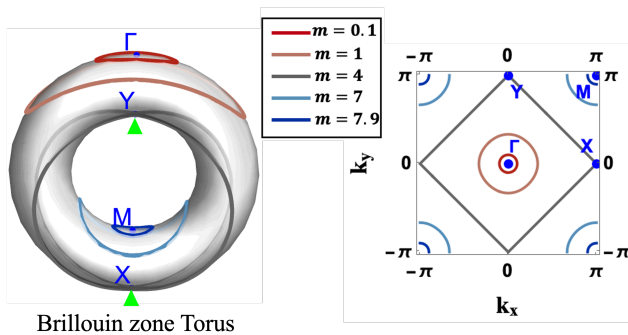


Figure 3. Distribution of the BIS for different mass terms m on the 2D Brillouin zone torus (left) and the Brillouin zone plane (right).

rounded by which closed surfaces determines in which topological phase the system resides.

Therefore, to distinguish the topologies here, we need more refined indicators to label which closed surface encloses the origin. In fact, for the system with inversion symmetry, this indicator corresponds to the high-symmetry points in the Brillouin zone. To see this, we can examine the topological differences between the phases where $0 < m < 4$ and $4 < m < 8$. Fig.2(c-e) presents the bulk spectrum for $m = 1, 2$ and 6 , while the corresponding quasi-one-dimensional nanoribbon system spectrum is shown in Fig.2(f-h). In Fig.2(c-e), the color represents $|\psi_I|^2 - |\psi_{II}|^2$, with $\psi_{I/II}$ the two components of the spinor wave function. This visualization clearly indicates the band inversion surface (BIS) $d_z = 0$ in white. For $m = 1$ and 2 , the BIS encircle the Γ point, corresponding to edge states around the Γ point (red in Fig.2(f) and (g)). For $m = 6$, the BIS encircles the M point, with corresponding edge states around the M point (Fig.2(h)). In the cases of $m = 1$ and $m = 6$, the edge states have different momenta, resulting in the existence of helical edge states at their interface in Fig. 1(e) and (f).

To better visualize their topological differences, Fig.2(i-k) shows the distribution of $\mathbf{d}(\mathbf{k})$ in the Brillouin zone for $m = 1, 2$, and 6 . From the distribution of $\mathbf{d}(\mathbf{k})$, we can identify skyrmion structures. Skyrmion, a concept from field theory[38], play an important role in magnetism[39–42] and topological classification due to its topological properties[33, 43, 44]. Previous studies have suggested a correlation between the number of skyrmions and the Chern number[43]. We can determine a skyrmion's position using BIS and topological charges. The topological charges, i.e., $d_x = d_y = 0$, appear at the Γ , M , X , and Y points. These are a result of the system's inversion symmetry, as will be proved later. For $m = 1$ and 2 , the BIS encircles the topological charge at the Γ point, corresponding to a skyrmion located at Γ . Conversely, for $m = 6$ [Fig.2(k)], the BIS encircles the topological charge at the M point, indicative of a skyrmion located at M .

In fact, skyrmions at different high-symmetry points can further classify the topology, as the origin being enclosed by different closed surfaces corresponds to skyrmions appearing

at these distinct high-symmetry points. To see this, we can examine how the skyrmion manifests on the surface $\mathbf{d}(\mathbf{k})$. Similar to skyrmions in the Brillouin zone, skyrmions can be identified by the BIS encircling a topological charge. Here, the topological charge, i.e., $d_x = d_y = 0$, corresponds to the intersection of the surface with the z -axis (marked in blue crosses in Fig.2(b)). The BIS is the plane $d_z = 0$ intersecting with the surface $\mathbf{d}(\mathbf{k})$ [yellow loop in the Fig.2(b)]. A structure where a topological charge is encircled by the BIS defines a complete skyrmion. For instance, in Fig. 2(b), the BIS encircles a charge located at the Γ point, indicating the presence of a skyrmion at the Γ point.

In our model, all charges appear at high-symmetry points. Below, we demonstrate that this is due to inversion symmetry. The two-dimensional inversion symmetry is written as $P = \hat{P} \otimes \hat{R}_{2D}$, where $\hat{P} = \sigma_z$ acts on the spin space and \hat{R}_{2D} is a 2D spatial operator acting on the real space $\mathbf{R} \rightarrow -\mathbf{R}$. For the system with preserved inversion symmetry: $\hat{P}H(k)\hat{P}^{-1} = H(-k)$. At the four high-symmetry points Λ_i , which are inversion-invariant points, we have $\hat{P}H(\Lambda_i)\hat{P}^{-1} = H(\Lambda_i)$, where $\{\Lambda_i\} = \{\Gamma(0, 0), M(\pi, \pi), X(\pi, 0), Y(0, \pi)\}$. Since $H(\Lambda_i) = \mathbf{d}(\Lambda_i) \cdot \hat{\sigma}$, we get $-d_{x/y}(\Lambda_i) = d_{x/y}(\Lambda_i) = 0$, indicating that topological charges must exist at these high-symmetry points. We define the Chern number contributed by the skyrmion at the high-symmetry point Λ_i as \mathbb{C}_{Λ_i} . Therefore, in the intervals $0 < m < 4$ and $4 < m < 8$, skyrmions appear at the Γ point and the M point, respectively, corresponding to $\mathbb{C}_{\Gamma} = 1$ and $\mathbb{C}_M = 1$.

In the surface $\mathbf{d}(\mathbf{k})$, lattice momentum \mathbf{k} is a latent variable. To better illustrate the topological classification based on high symmetry points, we directly observe the phase transitions from the Brillouin zone, which explicitly contains momentum information. Figure 3 shows the evolution of the BIS in the Brillouin zone as a torus and as a plane when m changes from 0.1 to 7.9 . It can be observed that at $m = 0.1$ and $m = 7.9$, the loops encircle the Γ point (red circle) and the M point (blue circle), respectively, corresponding to skyrmions located at the Γ point and the M point, defined as $\mathbb{C}_{\Gamma} = 1$ and $\mathbb{C}_M = 1$.

To transform a loop on the torus that encircles the Γ point into one that encircles the M point, a straightforward method is to translate the loop on the surface. However, this will inevitably cause the loop to touch the Γ point, which physically corresponds to the gap closing and reopening at the Γ point. Additionally, when translating the loop, there is no guarantee that the Γ point remains the inversion center of the loop, thus breaking the inversion symmetry of the system.

However, the periodicity of the 2D Brillouin zone gives it a toroidal geometric structure, leading to an alternative method to transform the loop from encircling the Γ point to encircling the M point, without gap close at Γ point and preserves inversion symmetry throughout the process. By increasing the radius of the loop (corresponding to increasing the mass term m in the model), the loop can grow until it touches itself on the opposite side of the torus (marked in green triangles). This discontinuous change corresponds to a topological transition,

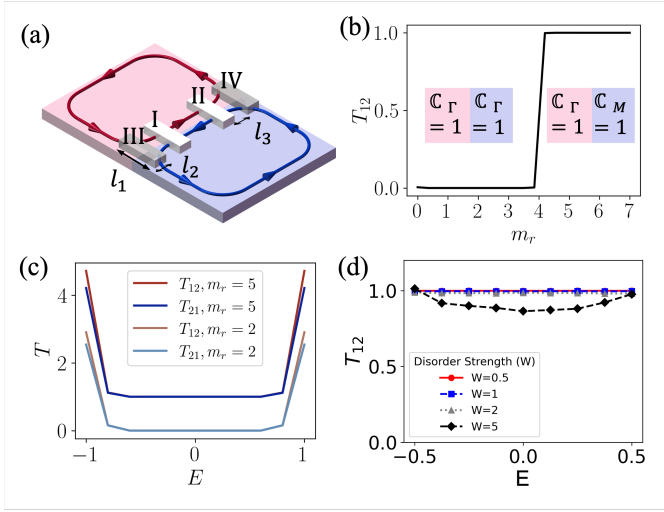


Figure 4. (a) Schematic of the transport device: Measurement ports are labeled I and II, while protective ports are labeled III and IV. The geometric parameters are $l_1 = 10$, $l_2 = 5$, and $l_3 = 10$. (b) Dependence of T_{12} on m_r at energy $E = 0$. The inset marks the Chern numbers \mathbb{C} base on high-symmetry points of the left and right halves when m_r is in the intervals 0 to 4 and 4 to 7, respectively. (c) Plots of T_{12} and T_{21} versus energy for different values of m_r . (d) T_{12} versus energy for different disorder strengths W with $m_r = 5$

and after this transition, the loop becomes one that encircles the M point. The phase transition here relies on the toroidal structure of the Brillouin zone. Considering that any two-dimensional periodic lattice system features a Brillouin zone with a toroidal structure, such phase transitions are likely to be universally present.

The helical modes at the interface can be detected through transport measurements. We constructed the rectangular system shown in Fig.4(a), with dimensions $L_x = 100$ and $L_y = 50$. The system is divided into left and right parts at $i_x = 50$, with different mass term. The mass term for the left part are set to $m_l = 1$, while the mass term for the right part set to m_r . The ports are attached on the interface of the two blocks, labeled as I-IV. Ports III and IV are grounded to prevent the influence of the outer chiral channel. The transmission probability between ports I and II reflects the number of channels at the interface.

The transmission T between port n and port m can be derived by using non-equilibrium Green's function[45–50]: $T_{mn}(E) = \text{Tr} [\Gamma_n \mathbf{G}^R \Gamma_m \mathbf{G}^A]$ where $\Gamma_{n/m}$ represents the line-width function of the n/m -th port, which is a constant under the wide-band approximation. The retarded Green's function is defined as: $\mathbf{G}^R(E) = [\mathbf{G}^A]^\dagger = [(E + i0^+) \mathbf{I} - \mathbf{H} - \sum_n \Sigma_n^R]^{-1}$. The self-energy term is given by: $\Sigma_n^R = -\frac{i}{2} \Gamma_n$.

Figure 4(b) shows the variation of T_{12} as m_r increases. At $m_r = 4$, T_{12} suddenly changes from 0 to 1. This indicates that around $m = 4$, as the right side transitions from the $\mathbb{C}_\Gamma = 1$ phase to the $\mathbb{C}_M = 1$ phase, gapless helical modes appear

at the interface because the right and left sides belong to different topological phases. Figure 4(c) shows the transmission probabilities T_{12} and T_{21} as a function of the energy for different m_r . When $m_r = 2$, both sides of the system belong to $\mathbb{C}_\Gamma = 1$, and no gapless states are present at the interface, resulting in a transmission probability of 0 within the gap. However, when $m_r = 5$, the left and right sides are at the different topological phases, leading to the presence of the helical transport channel at the interface and $T_{12} = T_{21} = 1$.

To investigate the robustness of the helical modes at the interface, the on-site energies at the Hamiltonian in Eq.(1) are added with a disorder term $\epsilon_i \sigma_0$ with[51–54]

$$\epsilon_i = \sum_j \tilde{\epsilon}_j e^{-|\mathbf{r}_{ij}|^2/2\eta^2} / \sqrt{\sum_j e^{-|\mathbf{r}_{ij}|^2/2\eta^2}},$$

Here $\tilde{\epsilon}_j$ is uniformly distributed in the interval $[-W/2, W/2]$, where W the disorder strength. $|\mathbf{r}_{ij}|$ denotes the distance between site i and j , while η describes the correlation length of the disorder. In the numerical calculations, we use a long-range disorder with $\eta = 1.5a$, where a is the lattice constant, set to 1 in this context. The transmission coefficient $T_{12}(E)$ is averaged over 100 different disorder configurations for each value of W . Figure 4(d) illustrates $T_{12}(E)$ under varying W . It remains quantized even when $W = 1$, indicating effective suppression of backscattering. This demonstrates the robustness of the topologically protected counter-propagating helical modes at the interface, supported respectively by $\mathbb{C}_\Gamma = 1$ and $\mathbb{C}_M = 1$.

In addition to photonic systems, our classification theory is broadly applicable to all inversion-symmetric systems with a Brillouin zone, including cold atoms, acoustic, and mechanical systems. In fact, the Qi-Wu-Zhang model, which closely resembles the model described by Eq.(2) in this study, has already been realized in Bose-Einstein condensates [55–58] and optical Raman lattices [59]. Additionally, BIS, which determines the position of skyrmions, can be both observed and adjusted experimentally [57], and recent advancements in real-space detection based on ultracold atoms have enabled the experimental observation of topological modes at the interface between two distinct topological systems [60].

In summary, we propose that for systems with inversion symmetry, those with the same Chern number can be further classified based on the high-symmetry points where the skyrmions are located. On the torus surface of the Brillouin zone, the topological transition between different phases with the same Chern number involves that the loop of the BIS touches itself and reopens. Gapless helical states appear at the interface between different topological phases, providing counter-propagating transport channels. These transport channels are topologically protected and robust against disorder, offering additional avenues for controlling topological optical transport. Furthermore, our work has deepened the understanding of the topological phases of Chern insulators with inversion symmetry.

Y.-H. W. is grateful to Jiayu Li, Ming Gong, Fajie Wang,

Yucheng Wang, Chao Yang and Ludan Zhang for fruitful discussions. This work was financially supported by the National Natural Science Foundation of China (Grant No. 12374034 and No. 11921005), the Innovation Program for Quantum Science and Technology (2021ZD0302403), and the Strategic priority Research Program of Chinese Academy of Sciences (Grant No. XDB28000000). We also acknowledge the Highperformance Computing Platform of Peking University for providing computational resources.

* Corresponding author: sunqf@pku.edu.cn.

- [1] F. D. M. Haldane and S. Raghu, *Phys. Rev. Lett.* **100**, 013904 (2008).
- [2] S. H. Mousavi, A. B. Khanikaev, and Z. Wang, *Nat Commun* **6**, 8682 (2015).
- [3] S. K. Sridhar, S. Ghosh, D. Srinivasan, A. R. Miller, and A. Dutt, *Nat. Phys.* **20**, 843 (2024,5).
- [4] Z. Wang, Y. D. Chong, J. D. Joannopoulos, and M. Soljačić, *Phys. Rev. Lett.* **100**, 013905 (2008).
- [5] L.-H. Wu and X. Hu, *Phys. Rev. Lett.* **114**, 223901 (2015).
- [6] J. Jiang, F. Tang, X. C. Pan, H. M. Liu, X. H. Niu, Y. X. Wang, D. F. Xu, H. F. Yang, B. P. Xie, F. Q. Song, P. Dudin, T. K. Kim, M. Hoesch, P. K. Das, I. Vobornik, X. G. Wan, and D. L. Feng, *Phys. Rev. Lett.* **115**, 166601 (2015).
- [7] Z. Wang, Y. Chong, J. D. Joannopoulos, and M. Soljačić, *Nature* **461**, 772 (2009,10).
- [8] S. A. Skirlo, L. Lu, Y. Igarashi, Q. Yan, J. Joannopoulos, and M. Soljačić, *Phys. Rev. Lett.* **115**, 253901 (2015).
- [9] S. Mittal, V. V. Orre, D. Leykam, Y. D. Chong, and M. Hafezi, *Phys. Rev. Lett.* **123**, 043201 (2019).
- [10] J.-W. Dong, X.-D. Chen, H. Zhu, Y. Wang, and X. Zhang, *Nature Mater* **16**, 298 (2017,3).
- [11] J. Lu, C. Qiu, W. Deng, X. Huang, F. Li, F. Zhang, S. Chen, and Z. Liu, *Phys. Rev. Lett.* **120**, 116802 (2018).
- [12] F. Gao, H. Xue, Z. Yang, K. Lai, Y. Yu, X. Lin, Y. Chong, G. Shvets, and B. Zhang, *Nat. Phys.* **14**, 140 (2018,2,1).
- [13] J. Noh, S. Huang, K. P. Chen, and M. C. Rechtsman, *Phys. Rev. Lett.* **120**, 063902 (2018).
- [14] H. Yang, J. Xu, Z. Xiong, X. Lu, R.-Y. Zhang, H. Li, Y. Chen, and S. Zhang, *Phys. Rev. Lett.* **127**, 043904 (2021).
- [15] X. Yin, Z. Ye, J. Rho, Y. Wang, and X. Zhang, *Science* **339**, 1405 (2013,3,22).
- [16] M. Hafezi, E. A. Demler, M. D. Lukin, and J. M. Taylor, *Nat. Phys.* **7**, 907 (2011,11).
- [17] K. Y. Bliokh, D. Smirnova, and F. Nori, *Science* **348**, 1448 (2015,6,26).
- [18] D. Leykam, S. Mittal, M. Hafezi, and Y. D. Chong, *Phys. Rev. Lett.* **121**, 023901 (2018).
- [19] C.-K. Chiu, J. C. Y. Teo, A. P. Schnyder, and S. Ryu, *Rev. Mod. Phys.* **88**, 035005 (2016).
- [20] M. C. Rechtsman, J. M. Zeuner, Y. Plotnik, Y. Lumer, D. Podolsky, F. Dreisow, S. Nolte, M. Segev, and A. Szameit, *Nature* **496**, 196 (2013,4).
- [21] K. Fang, Z. Yu, and S. Fan, *Nature Photon* **6**, 782 (2012,11).
- [22] A. Bansil, H. Lin, and T. Das, *Rev. Mod. Phys.* **88**, 021004 (2016).
- [23] M. Aidelsburger, S. Nascimbene, and N. Goldman, *C. R. Physique Quantum Simulation / Simulation Quantique*, **19**, 394 (2018).
- [24] H. C. Wu, H. S. Xu, L. C. Xie, and L. Jin, *Phys. Rev. Lett.* **132**, 083801 (2024).
- [25] I. T. Rosen, E. J. Fox, X. Kou, L. Pan, K. L. Wang, and D. Goldhaber-Gordon, *npj Quantum Materials* **2**, 1 (2017).
- [26] Y.-F. Zhao, R. Zhang, J. Cai, D. Zhuo, L.-J. Zhou, Z.-J. Yan, M. H. W. Chan, X. Xu, and C.-Z. Chang, *Nature Communications* **14**, 770 (2023).
- [27] C. Zhang, T. Zhu, S. Kahn, T. Soejima, K. Watanabe, T. Taniguchi, A. Zettl, F. Wang, M. P. Zaletel, and M. F. Crommie, *Nat. Phys.* **20**, 951 (2024).
- [28] M. Z. Hasan and C. L. Kane, *Rev. Mod. Phys.* **82**, 3045 (2010).
- [29] X.-L. Qi and S.-C. Zhang, *Rev. Mod. Phys.* **83**, 1057 (2011).
- [30] J. Wang, B. Lian, and S.-C. Zhang, *Phys. Rev. B.* **89**, 085106 (2014).
- [31] M. Liu, W. Wang, A. R. Richardella, A. Kandala, J. Li, A. Yazdani, N. Samarth, and N. P. Ong, *Science Advances* **2**, e1600167 (2016,7).
- [32] Q. Yan, H. Li, H. Jiang, Q.-F. Sun, and X. C. Xie, *Science Advances* **10**, eado4756 (2024,6,7).
- [33] X.-L. Qi, Y.-S. Wu, and S.-C. Zhang, *Phys. Rev. B.* **74**, 085308 (2006).
- [34] S.-Q. Shen, *Topological Insulators: Dirac Equation in Condensed Matters*, Springer Series in Solid-State Sciences, Vol. 174 (Springer Berlin Heidelberg, Berlin, Heidelberg, 2012).
- [35] S.-Q. SHEN, W.-Y. SHAN, and H.-Z. LU, *SPIN* **01**, 33 (2011,6).
- [36] .
- [37] J. K. Asbóth, L. Oroszlány, and A. Pályi, *A Short Course on Topological Insulators*, Lecture Notes in Physics, Vol. 919 (Springer International Publishing, Cham, 2016).
- [38] T. Skyrme, *Nucl. Phys.* **31**, 556 (1962,3).
- [39] A. Bogdanov and A. Hubert, *J. Magn. Magn. Mater.* **138**, 255 (1994,12).
- [40] U. K. Röfler, A. N. Bogdanov, and C. Pfleiderer, *Nature* **442**, 797 (2006).
- [41] S. Mühlbauer, B. Binz, F. Jonietz, C. Pfleiderer, A. Rosch, A. Neubauer, R. Georgii, and P. Böni, *Science* **323**, 915 (2009).
- [42] X. Z. Yu, Y. Onose, N. Kanazawa, J. H. Park, J. H. Han, Y. Matsui, N. Nagaosa, and Y. Tokura, *Nature* **465**, 901 (2010,6).
- [43] K. Björnson and A. M. Black-Schaffer, *Phys. Rev. B.* **89**, 134518 (2014).
- [44] F. Loder, A. P. Kampf, T. Kopp, and D. Braak, *Phys. Rev. B.* **96**, 024508 (2017).
- [45] C.-H. Wang and J. M. Taylor, *Phys. Rev. B* **94**, 155437 (2016).
- [46] G. Salerno, H. M. Price, M. Lebrat, S. Häusler, T. Esslinger, L. Cormann, J.-P. Brantut, and N. Goldman, *Phys. Rev. X* **9**, 041001 (2019).
- [47] M. Büttiker, *Phys. Rev. B* **38**, 9375 (1988).
- [48] D. S. Fisher and P. A. Lee, *Phys. Rev. B* **23**, 6851 (1981).
- [49] R. Landauer, *Philos. Mag.* **21**, 863 (1970).
- [50] M. Gong, M. Lu, H. Liu, H. Jiang, Q.-F. Sun, and X. C. Xie, *Phys. Rev. B* **102**, 165425 (2020).
- [51] T. Kawarabayashi, Y. Hatsugai, and H. Aoki, *Phys. Rev. Lett.* **103**, 156804 (2009).
- [52] S.-g. Cheng, J. Zhou, H. Jiang, and Q.-F. Sun, *New J. Phys.* **18**, 103024 (2016).
- [53] S.-g. Cheng, H. Zhang, and Q.-f. Sun, *Phys. Rev. B.* **83**, 235403 (2011).
- [54] N.-X. Yang, Y.-F. Zhou, P. Lv, and Q.-F. Sun, *Phys. Rev. B.* **97**, 235435 (2018).
- [55] B.-Z. Wang, Y.-H. Lu, W. Sun, S. Chen, Y. Deng, and X.-J. Liu, *Phys. Rev. A.* **97**, 011605 (2018).
- [56] W. Sun, B.-Z. Wang, X.-T. Xu, C.-R. Yi, L. Zhang, Z. Wu, Y. Deng, X.-J. Liu, S. Chen, and J.-W. Pan, *Phys. Rev. Lett.*

- [121](#), [150401](#) (2018).
- [57] W. Sun, C.-R. Yi, B.-Z. Wang, W.-W. Zhang, B. C. Sanders, X.-T. Xu, Z.-Y. Wang, J. Schmiedmayer, Y. Deng, X.-J. Liu, S. Chen, and J.-W. Pan, [Phys. Rev. Lett.](#) **121**, [250403](#) (2018).
- [58] Z. Wu, L. Zhang, W. Sun, X.-T. Xu, B.-Z. Wang, S.-C. Ji, Y. Deng, S. Chen, X.-J. Liu, and J.-W. Pan, [Science](#) **354**, [83](#) (2016).
- [59] M.-C. Liang, [Phys. Rev. Res.](#) **5** (2023), [10.1103/PhysRevResearch.5.L012006](#).
- [60] C. Braun, R. Saint-Jalm, A. Hesse, J. Arceri, I. Bloch, and M. Aidelsburger, [Nat. Phys.](#) **20**, [1306](#) (2024,8).